

Statics Modeling of Discrete Joint Surgical Probes with Tendon-based Stiffening

Yilin Cai, Andrew L. Orehov, Howie Choset

Abstract—Minimally-invasive surgical (MIS) robots can reduce post-operative pain and complications but must be able to follow tortuous paths to reach deep into the body. Our prior work on a MIS robot called the “highly articulated robot probe” (HARP) enabled follow-the-leader motion using two concentrically driven segmented tubes that alternate between locking and advancing each segment. By varying the tendon tension, HARP can be steerable during insertion for deep unsupported access and then become rigid to provide a stable platform at the site of clinical intervention. To design and control such robots, a statics model is essential, but existing statics models do not predict HARP’s payload capacity for arbitrary 3D shapes and external loads. To address this need, this paper presents a 3D statics model that includes link-to-link friction effects and external loading conditions and enables the maximum admissible external load to be determined for any given robot shape. We investigate how the payload capacity is influenced by both the robot’s shape and the actuation tendon forces and validate the statics model experimentally on a prototype HARP platform. Our results demonstrate that the proposed model can predict the payload capacity with a mean error below 0.19 N and a max error below 0.36 N. The model presented in this paper will enable future design, control, and planning methods with HARP robots to optimize their payload capacity for MIS tasks.

I. INTRODUCTION

The use of minimally invasive tools has the potential to reduce post-operative pain for patients. Naturally, we want these tools to be strong enough to exert the necessary forces on the anatomy, but soft enough so as to not cause collateral damage [1], [2]. Recent work in highly articulated robots, or so-called snake robots, have extended the reach of minimally invasive devices in that a physician can steer the robot deeper into the anatomy, reaching locations not necessarily within line of sight of the small surgical incision [3]. The problem is that the tortuous paths a highly articulated probe may follow could cause a loss of stiffness. This work develops a model for the statics of a particularly “highly articulated robot probe” (HARP), as shown in Fig. 1a. With this model in-hand, one can better design and control such a robot.

The HARP architecture consists of two concentric tendon-driven segmented snakes, the inner snake and outer snake, where each snake consists of a series of discrete rigid links [4]. By varying the actuation tendon tension of one snake and relying on the link-to-link friction, each snake can change from being steerable to being rigid. When the snake is steerable, the snake’s steering angle can be adjusted. By alternating the state of each snake in an opposing step-wise

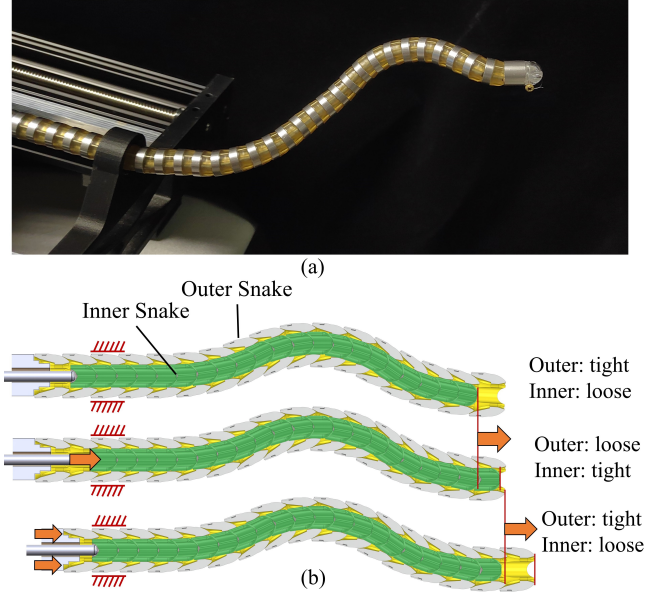


Fig. 1. The HARP. (a) A prototype of the HARP platform. (b) The “follow-the-leader” behavior achieved by alternating which snake is rigid/loose and advancing/steering the snakes in a step-wise fashion.

fashion, a “follow-the-leader” behavior can be achieved, as shown in Fig. 1b.

A variety of mechanical design architectures have been presented in prior work on surgical robots [5]–[7]. In the context of prior designs, the HARP system is tendon-actuated and discrete-jointed, similar to [8]–[10], and is related to [11] in its use of actuation tendon tension to adjust its stiffness/heading. HARP is unique in being both highly articulated and able to vary its stiffness while being under-actuated. HARP’s ability to follow arbitrary curves in 3D space, unsupported, can enable deeper surgical access. Furthermore, its ability to vary its stiffness can allow it to navigate deep into the body while still having the payload capacity to manipulate tissue with lower deflections than a typical flexible continuum robot [5].

The combination of these features makes the HARP design architecture a favorable candidate for endoluminal/transluminal procedures where forceful manipulation is needed. For better robot control in such procedures, a statics model is essential to predict the HARP’s payload capacity for any arbitrary shape. Such a statics model would enable one to plan paths within the body to maximize payload, and to furthermore modulate the maximum force direction online by varying the actuation tendon tensions. As reviewed in [5], [7], many prior works have presented statics models for

Y. Cai, A. L. Orehov, and H. Choset are with the Robotics Institute at Carnegie Mellon University, Pittsburgh, PA (yilinc, aorekhov, choset) @andrew.cmu.edu

various surgical manipulator architectures, including rigid-link devices [12], [13] and continuum devices [14]–[16]. However, most of these prior works do not apply to the HARP robot due to its unique follow-the-leader actuation mechanism. For the HARP robot, the required actuation forces in the straight configuration were provided in [4]. In [17], a model for a robot similar to HARP was presented, but the validation was limited to a single configuration, the model did not capture the ability of HARP to support torsional moments, and the payload capacity was not considered for any arbitrary shape.

To address these limitations in prior works, this paper presents a 3D statics model for one tendon-actuated snake (the outer snake) of HARP. We focus on the outer snake of HARP because, due to its three actuation tendons and larger radius, it provides the majority of HARP’s payload capacity once the target site is reached. Our proposed model includes the effect of link geometry, link-to-link friction, actuation tendon forces, and external forces applied to the robot. We show how the model can be used to predict the maximum admissible external load (i.e. payload) for any 3D robot shape. Finally, we experimentally validate the statics model and demonstrate the ability to modulate the payload capacity by varying the individual actuation tendon tensions.

II. STATICS MODEL FORMULATION

In this section, we present a statics model for the outer segment of HARP, including the effect of link-to-link friction and external loading. We first present the kinematic equations of the robot. We then present the statics model, including the force/moment equilibrium equations and a simplified Coulomb friction contact model to describe link-to-link friction. Finally, we show how we use the statics model to numerically solve for the maximum payload that the robot can support without resulting in slip between the links.

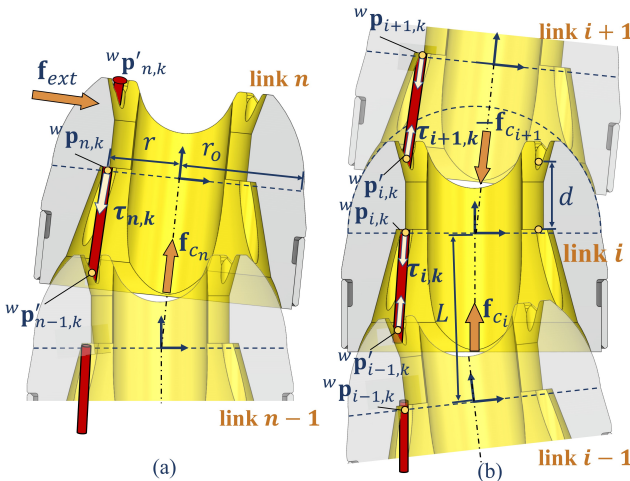


Fig. 2. Kinematics diagram for the HARP outer segment. (a) Distal link at the tip of the snake robot. (b) Middle link i and its two adjacent links along the body of the snake robot.

A. Robot Kinematics

We assume the robot has n links with three tendon channels 120° apart circumferentially. The kinematic representation of two adjacent links is shown in Fig. 2a. We define the body frame of link $i \in 1 \cdots n$ as a frame attached to the link’s geometric center. The k^{th} tendon ($k = 1, 2, 3$) passes into and out of the channel of link i at the points ${}^b\mathbf{p}_{i,k}$ and ${}^b\mathbf{p}'_{i,k}$, respectively. These two points are expressed in the body frame of link i :

$${}^b\mathbf{p}_{i,k} = \left[0, r \cos\left(\frac{4k-7}{6}\pi\right), r \sin\left(\frac{4k-7}{6}\pi\right) \right]^T \quad (1)$$

$${}^b\mathbf{p}'_{i,k} = \mathbf{p}_{i,k} + [d, 0, 0]^T \quad (2)$$

where k is the index of the tendon number, r is the distance from the center of the tendon channel to the link center, and d is the length of the link channel.

Following [18], the relative rotation between link $i-1$ and link i is represented by a bending angle ϕ_i and a bending direction angle θ_i . This provides the homogeneous transformation matrix between the two links:

$${}^{i-1}\mathbf{T}_i = \begin{bmatrix} {}^{i-1}\mathbf{R}_i & {}^{i-1}\mathbf{t}_i \\ \mathbf{0} & 1 \end{bmatrix} \in SE(3) \quad (3)$$

$$\begin{aligned} {}^{i-1}\mathbf{R}_i &= \mathbf{R}_x(\theta_i)\mathbf{R}_y(\phi_i)\mathbf{R}_x(-\theta_i) \in SO(3) \\ {}^{i-1}\mathbf{t}_i &= {}^{i-1}\mathbf{R}_i [L \ 0 \ 0]^T \in \mathbb{R}^3 \end{aligned} \quad (4)$$

The matrices \mathbf{R}_x and \mathbf{R}_y are the rotation matrices that rotate a 3-D vector about the x -axis and y -axis, respectively, and L is the length of each link. The homogeneous transformation matrix between any two links’ body frames is given by:

$${}^m\mathbf{T}_i = \prod_{j=m+1}^i {}^{j-1}\mathbf{T}_j \in SE(3) \quad (5)$$

We use ${}^m\mathbf{T}_i$ to transform the vertices where the tendons pass into and out of the link’s channel into any frame m , e.g. ${}^m\bar{\mathbf{p}}_{i,k} = {}^m\mathbf{T}_i {}^b\bar{\mathbf{p}}_{i,k}$, where ${}^m\bar{\mathbf{p}}_{i,k} = [{}^m\mathbf{p}_{i,k} \ 1]^T$.

B. Equilibrium Equations

We now consider the forces and moments applied to a single link. For the distal link n , shown in Fig. 2a, the forces applied to the link include the actuation tendon tensions, the external force applied to the link, the contact force from link $n-1$, and the force due to gravity. The actuation tendon tensions are given by:

$$\tau_{n,k} = T_k \frac{{}^w\mathbf{p}_{n,k} - {}^w\mathbf{p}'_{n-1,k}}{\|{}^w\mathbf{p}_{n,k} - {}^w\mathbf{p}'_{n-1,k}\|} \in \mathbb{R}^3 \quad (6)$$

where T_k is the tension on the k^{th} tendon, and ${}^w\mathbf{p}_{n,k}$ and ${}^w\mathbf{p}'_{n,k}$ are the vertices of the tendon channel expressed in the world frame (assumed here to be at the center of the base link). Here we assume the actuation tendon tension is constant along the link channels. The external force is defined as $\mathbf{f}_{ext} = F_{ext}\hat{\mathbf{n}}_{ext}$, where F_{ext} is the magnitude of the external force and $\hat{\mathbf{n}}_{ext}$ is the unit vector defining the external force direction. The contact force from link $n-1$ is

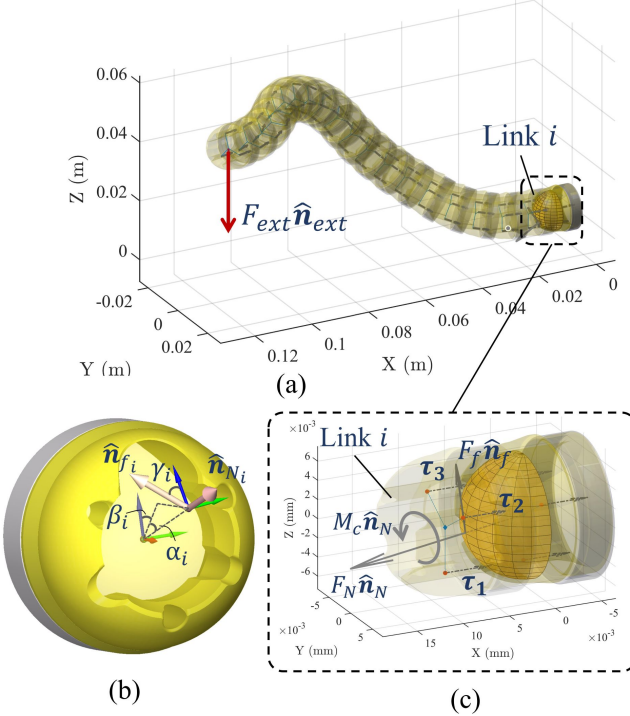


Fig. 3. The static force diagram for the HARP robot. (a) A 20-link HARP robot with an external force applied to the tip. (b) The direction of the normal reaction force and friction force between the two-link surfaces. (c) All forces and moments applied to link i .

given by $\mathbf{f}_{c_n} = F_{c_n}\hat{\mathbf{n}}_{c_n}$, where F_c is the magnitude and $\hat{\mathbf{n}}_c$ is the unit vector defining the contact force direction. Finally, the gravity force is similarly given by $\mathbf{f}_{g_n} = F_{g_n}\hat{\mathbf{n}}_g$, where F_g is the magnitude and $\hat{\mathbf{n}}_g$ is the unit direction. We assume the external force is applied on the center point of the distal link frame and expressed in the world frame. We then have the force equilibrium equations of the distal link as:

$$\sum_{k=1}^3 \boldsymbol{\tau}_{n,k} + \mathbf{f}_{c_n} + \mathbf{f}_{ext} + \mathbf{f}_{g_n} = \mathbf{0} \quad (7)$$

For a middle link, shown in Fig. 2b, there are additional forces applied to the link. These include the contact force from the previous link and the actuation tendon forces from the two adjacent links. The net forces from the actuation tendons are given by:

$$\begin{aligned} \boldsymbol{\tau}_{i,k}^{\text{net}} &= \boldsymbol{\tau}_{i,k} - \boldsymbol{\tau}_{i+1,k} \\ &= T_k \frac{^w\mathbf{p}_{i,k} - ^w\mathbf{p}'_{i-1,k}}{\| ^w\mathbf{p}_{i,k} - ^w\mathbf{p}'_{i-1,k} \|} + T_k \frac{^w\mathbf{p}'_{i,k} - ^w\mathbf{p}_{i+1,k}}{\| ^w\mathbf{p}'_{i,k} - ^w\mathbf{p}_{i+1,k} \|} \end{aligned} \quad (8)$$

The force equilibrium equations for the middle link i are therefore:

$$\sum_{k=1}^3 \boldsymbol{\tau}_{i,k}^{\text{net}} + \mathbf{f}_{c_i} - \mathbf{f}_{c_{i+1}} + \sum_{k=1}^n \mathbf{f}_{g_k} = \mathbf{0} \quad (9)$$

By listing the force equilibrium equations (7) and (9) from link i to n , we can show through cancellation of contact force and actuation tendon terms that the force equilibrium for any link i is:

$$\sum_{k=1}^3 \boldsymbol{\tau}_{i,k} + \mathbf{f}_{ext} + \mathbf{f}_{c_i} + \sum_{k=1}^n \mathbf{f}_{g_k} = \mathbf{0} \quad (10)$$

Similarly, we can derive all the moments applied to the link i . Since the link i is in contact with its adjacent links on a spherical surface, the rotation center of link i is the origin of link $i-1$'s body frame. We have the moment equilibrium about its rotation center as:

$$\sum_{k=1}^3 \mathbf{r}_{k_i} \times \boldsymbol{\tau}_{i,k} + \mathbf{m}_{ext} + \mathbf{m}_{c_i} + \mathbf{m}_{g_i} = \mathbf{0} \quad (11)$$

where \mathbf{r}_{k_i} is the vector from the rotation center to point ${}^w\mathbf{p}_{i,k}$, $\mathbf{m}_{ext} = \mathbf{r}_{ext} \times F_{ext}\hat{\mathbf{n}}_{ext}$ is the moment caused by the external force, \mathbf{r}_{ext} is a vector from the rotation center to the location at which the external force is applied, \mathbf{m}_{c_i} is the moment from link $i-1$ through the contact surface, and $\mathbf{m}_{g_i} = \mathbf{r}_i \times F_g\hat{\mathbf{n}}_{g_i}$ gives the moment due to gravity. Now, as shown in Fig. 3 (a), for any link i we can describe the statics using these force and moment equilibrium equations.

C. Link-to-Link Friction Contact Model

We now formulate the contact force \mathbf{f}_{c_i} and the contact moment \mathbf{m}_{c_i} between two links. We model the two links as a ball and socket with friction. Following prior work on modeling of spherical joints [19]–[21], we note the ball and the socket will elastically deform under load to produce a small area of contact. Therefore, the interaction between links is determined by the pressure distribution and tangential friction force distribution over the contact area. The moment about the ball joint's rotation center caused by this friction force distribution will help resist the external torsional moments. As described in [21], the total friction moment over the contact area can be divided into two components: 1) a component acting about the axis perpendicular to the normal reaction force direction, 2) a component acting about the axis coincident with the normal reaction force direction.

Here we seek a simplified model to approximate the complex friction force distribution between the link surfaces. To this end, we model the contact between the two spherical surfaces as a single point contact. The contact point on the spherical surface depends on the steering angle and the direction of external load. Applied at each contact point are a normal reaction force, a perpendicular friction force, and a torsional friction moment about the normal reaction force direction. This combination of friction force and torsional friction moment at the point of contact is meant to approximate the two friction moment components in [21].

As shown in Fig. 3(b), in the base link frame, the direction of the normal reaction force is defined by a unit vector $\hat{\mathbf{n}}_{N_i} = [\sin \alpha_i, \cos \alpha_i \sin \beta_i, \cos \alpha_i \cos \beta_i]^T$, where α_i is the angle between $\hat{\mathbf{n}}_{N_i}$ and the $y-z$ plane, β_i is the angle between $\hat{\mathbf{n}}_{N_i}$ and the z -axis projected to the $y-z$ plane. These variables also allow us to define a contact frame whose origin is at the contact point and whose x -axis is aligned with $\hat{\mathbf{n}}_{N_i}$:

$${}^b\mathbf{T}_{c_i} = \begin{bmatrix} {}^b\mathbf{R}_{c_i} & {}^b\mathbf{R}_{c_i}[r_o, 0, 0]^T \\ \mathbf{0} & 1 \end{bmatrix} \quad (12)$$

where ${}^b\mathbf{R}_{c_i} = \mathbf{R}_x(-\beta_i)\mathbf{R}_y(\alpha_i - \frac{\pi}{2})$. The unit vector defining the direction of the friction force is perpendicular to $\hat{\mathbf{n}}_{N_i}$ and

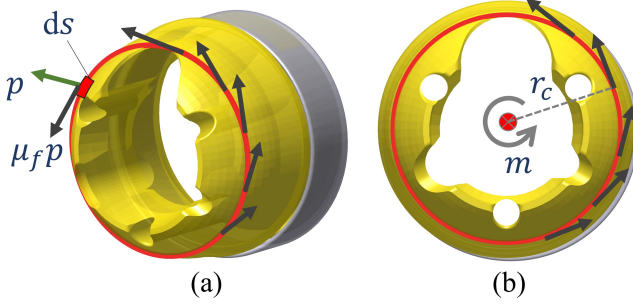


Fig. 4. The contact ring to estimate the torsional friction coefficient μ_m . (a) Normal pressure p and unit friction force $\mu_f p$ applied on the infinitesimal arc element ds . (b) Unit moment about the center axis applied by the infinitesimal arc element ds .

is given by:

$$\hat{\mathbf{n}}_{f_i} = {}^b\mathbf{R}_{c_i} [0, -\cos \gamma_i, \sin \gamma_i]^T \quad (13)$$

where γ_i indicates the angle between $\hat{\mathbf{n}}_f$ and the contact frame's z -axis, as shown in Fig. 3(c). The contact force is therefore given by:

$$\mathbf{f}_{c_i} = F_{N_i} \hat{\mathbf{n}}_{N_i} + F_{f_i} \hat{\mathbf{n}}_{f_i} \quad (14)$$

where F_{N_i} and F_{f_i} are the magnitude of the normal reaction force and friction force, respectively. Under the assumption of static Coulomb friction, the friction force must satisfy $F_{f_i} \leq \mu_f F_{N_i}$, where μ_f is the static coefficient of friction.

Similarly, the torsional moment due to friction is given by:

$$\mathbf{m}_{c_i} = \mathbf{m}_{f_i} + \mathbf{m}_{t_i} \quad (15)$$

where $\mathbf{m}_{f_i} = r_o \hat{\mathbf{n}}_{N_i} \times F_{f_i} \hat{\mathbf{n}}_{f_i}$ and r_o is the radius of the outer link, $\mathbf{m}_{t_i} = M_{t_i} \hat{\mathbf{n}}_{N_i}$ is the torsional friction moment about the axis coincident with the normal reaction force direction, and M_{t_i} is the magnitude of the torsional moment. The torsional friction moment must satisfy $M_{c_i} \leq \mu_m F_{N_i}$, where we define μ_m as the torsional coefficient of friction. We approximate μ_m by considering the ring of contact between two links, as shown in Fig. 4(a) and (b). We define p as the normal pressure in an infinitesimal arc element ds , where s is the arc length along the contact ring. We then define m as the moment about the normal force direction axis caused by the force of friction at ds . Then we have:

$$\frac{M_c}{F_N} = \frac{\int_s m ds}{\int_s p ds} \leq \frac{\int_s \mu_f p r_c ds}{\int_s p ds} = \mu_f r_c \quad (16)$$

where s is the arc length of the contact ring and r_c is the radius of the contact ring. With this approximation of the ratio between the normal force and the torsional friction moment, we define the torsional friction coefficient as $\mu_m = \mu_f r_c$. As expected, a snake with a larger radius will have a larger torsional friction moment and will be able to support larger torsion loads.

By substituting (14) and (15) into force equilibrium equation (10) and moment equilibrium equation (11), we give a full statics description of the HARP robot.

D. Solving for the Maximum Payload

We now use our proposed statics model to determine the maximum payload, defined as the maximum external force that can be exerted on the robot without causing a slip between any two links. Given a set of tendon tensions τ_k and a known external force direction, we first solve for the maximum payload for a particular link i . To do this, we start from 0 and increase F_{ext} in increments of 0.05 N. For each step in F_{ext} , we numerically solve the force and moment balance equations (10) and (11) for $F_{N_i}, F_{f_i}, \alpha_i, \beta_i, \gamma_i$, and M_{c_i} . As soon as either of the constraints $F_{f_i} \leq \mu_f F_{N_i}$ or $M_{c_i} \leq \mu_m F_{N_i}$ is violated, we take the previous value of F_{ext} as the maximum payload for link i .

To determine the payload capacity for the entire snake, we follow these steps for each link and take the minimum payload across all links as the payload of the entire snake. With this approach, we also determine the “weakest link” of the robot, i.e. the link which will fail first.

To numerically solve (10) and (11), we use the Levenberg–Marquardt solver via *fsove()* in MATLAB. In our current implementation on a desktop PC with a i7-11700 2.50 GHz CPU, solving for the payload takes roughly 2-3 seconds for one link and 45-55 seconds for the entire snake. We observed that successful convergence of the solver was sensitive to the initial guess, so we ran the solver with different random initial guesses until convergence. We also restarted the solver with a different initial guess if the magnitudes of the force F_{N_i} and moment M_{c_i} were not greater than zero. In our current implementation on a desktop PC with a i7-11700 2.50 GHz CPU, solving for the payload takes 2-3 seconds for one link and 45-55 seconds on average for the entire snake.

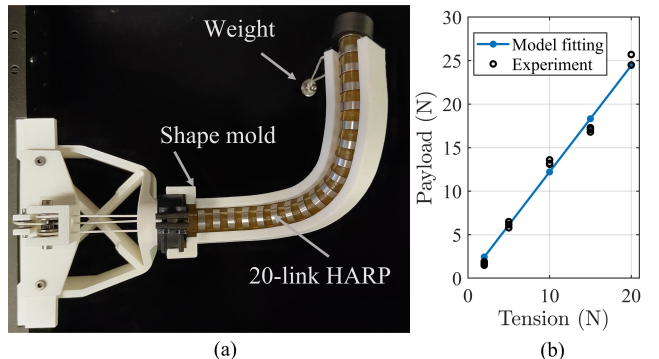


Fig. 5. Experiment setup and friction coefficient calibration. (a) Payload testing setup on a 20-link HARP robot. (b) Friction coefficient calibration results using only two links, with three experiments for each set of tendon tensions.

III. EXPERIMENTAL MODEL VALIDATION

In this section, the ability of the proposed statics model to predict the maximum payload is validated on a prototype HARP robot.

A. Experiment Setup and Friction Coefficient Calibration

Figure 5a shows the experiment setup for validating our model. The HARP robot has three actuation tendons controlling the outer snake, which has 20 links with a total length of

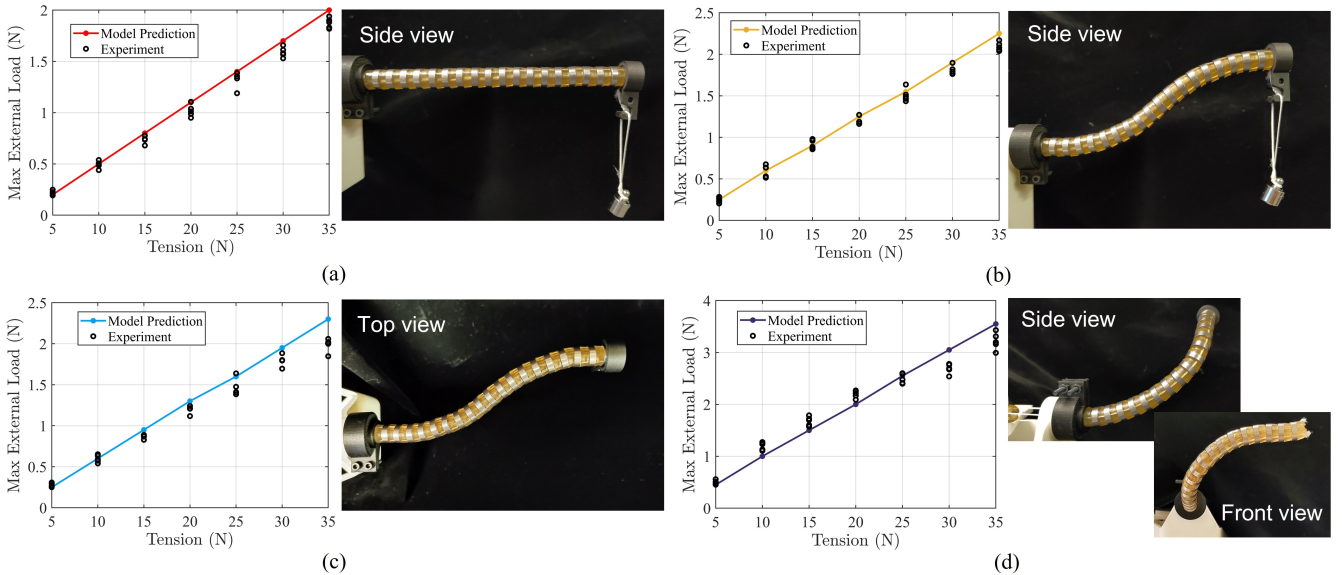


Fig. 6. Experimental validation of our payload capacity model for HARP for different tendon loads (with five experiments for each tendon load) and four different snake configurations: (a) straight configuration, (b) curved configuration in the horizontal plane, (c) curved configuration in the vertical plane, (d) non-planar spatial configuration.

170 mm and an outer diameter of 12.7 mm. The kinematic radius of the actuation tendons is 4.95 mm. A 3D-printed mold was used to set the ground-truth robot configuration, and the tendon tensions were maintained by hanging known weights on each tendon. After removing the mold, we then incrementally increased the force applied to the snake's tip (in increments of approximately 3 grams) by hanging known weights on the tip. We observed that the link slip happened suddenly when the applied force reached a certain value. For each test, we recorded the weight that caused the robot to slip and compared this experimentally determined payload capacity to our model prediction.

We used a similar (but using only two links) to calibrate the friction coefficient μ_f before we validated the full model. The static model is fitted to the experiment data using a least-squares fitting, with the results shown in Fig. 5b. The calibrated friction coefficient was 0.58, which is similar to the nominally estimated friction coefficient of 0.5 [4].

Potential sources of error in the experimental validations include small clearances between the 3D printed fixtures and the probe, deflections in the 3D printed base structure where the snake was mounted, and unmodeled tendon elasticity and friction between the actuation tendon and the snake's working channels.

B. Experimental Validation with Equal Tensions

The proposed statics model was verified on the four different snake shapes shown in Fig. 6: straight, horizontal S-shape, vertical S-shape, and a non-planar spatial shape. The three actuation tendons were set to the same tension, ranging from 5 N to 35 N at intervals of 5 N, and the process described above was used to experimentally determine the payload. The experiment was done five times for each set of applied tension loads. We then compared these

TABLE I
PAYLOAD CAPACITY MODELING ERROR WITH EQUAL TENSION

Shape	Mean Absolute Error	Max Error
Straight	0.07 N (3.73%)	0.13 N (6.73%)
Vertical S-shape	0.05 N (2.51%)	0.16 N (7.54%)
Horizontal S-shape	0.12 N (6.08%)	0.31 N (15.77%)
Non-planar Shape	0.19 N (6.10%)	0.36 N (11.23%)

experimentally determined payload capacities to our model's prediction.

As shown in Fig. 6, the payload capacity increases linearly with the actuation tension, matching what our model predicted. The mean and maximum payload capacity errors, as well as the error as a percent of the maximum payload for that particular configuration, are given in Table I. Over all experiments, our model predicted the payload capacity with a mean error below 0.20 N and a maximum error below 0.36 N. The mean error and the max error is smaller than 6.5% and 16% of the maximum payload for this configuration, respectively. As shown in Fig. 6, the experimentally determined payload could vary as much as 0.50 N for a single set of actuation tendon loads, so we believe our reported maximum error is reasonable to validate the proposed model.

The largest errors occurred with the non-planar curved shape. A potential explanation for this larger error is the additional difficulty for the non-planar shape in ensuring that all links are aligned when manually placing the snake into the 3D-printed mold. The effects of unmodeled friction loss in the actuation tendons, which our model does not account for, may also play a larger role in the non-planar spatial shape due to its higher curvature.

C. Experimental Validation with Non-equal Tension

Payload testings were also conducted by setting different tensions to the actuation tendons. We observed in both experiments and with our model that by setting the tension T_1 to be 5 N less than the other two tendons, the payload capacity can increase by up to 35.50% and 24.51% for the straight and vertically curved configurations, respectively. The mean and maximum payload capacity errors, as well as the error as a percent of the maximum payload for that particular configuration, are given in Table II. Our model had a mean error of 0.07 N (3.55%) and 0.06 N (2.43%) for the payload prediction of these two configurations, respectively. The maximum errors are 0.15 N (7.18%) and 0.18 N (8.01%), respectively.

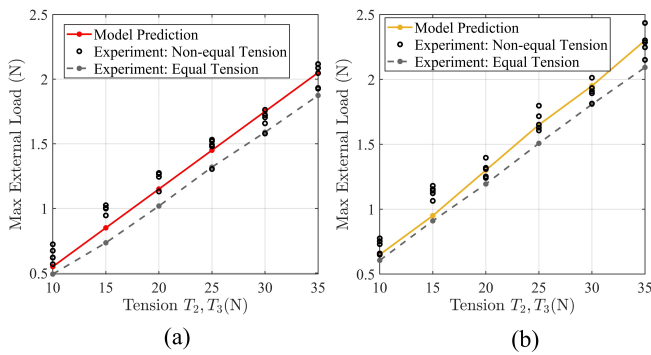


Fig. 7. Experimental validation of the payload capacity of HARP under non-equal tensions, where $T_2 = T_3 = T_1 + 5$ N in two configurations: (a) straight configuration. (b) curved configuration in vertical plane.

TABLE II
PAYLOAD CAPACITY MODELING ERROR WITH NON-EQUAL TENSION

Shape	Mean Absolute Error	Max Error
Straight	0.07 N (3.55%)	0.15 N (7.18%)
Vertical S-shape	0.06 N (2.43%)	0.18 N (8.01%)

These results show that we can in some cases increase the payload capacity by using non-equal tendon tensions and that our model can predict this increase in the payload capacity. We believe future controllers, together with the model presented herein, can actively adjust the individual actuation tendon tensions to maximize the payload, and in some configurations use reduced actuation tendon tensions without changing the payload capacity to reduce the stress and fatigue on the actuation tendons.

IV. CONCLUSIONS

In this paper, we have presented and experimentally validated a statics model for the HARP robot that predicts the robot's payload capacity for any robot shape and actuation tendon loads. We experimentally validated the model for four different robot shapes and two examples where the payload is increased when reducing the force on one actuation tendon. We believe our model will be useful for deriving future actuation controllers to maximize the payload capacity by

servoing the actuation tendon forces. Additionally, future motion planners can use this model to plan shapes that maximize the payload capacity.

The main limitation of this work is the computation cost of the solver, which is caused by the need to use multiple starts to find a solution and the need to solve the numerical optimization problem for every link in the snake. We believe code optimizations of our implementation can significantly improve the computation time. Analytical spherical joint models in the literature (despite not being directly suitable for determining the payload of our robot) could also be used to provide reasonable initial guesses to the solver and potentially remove the need for multiple starts.

Future work will include extension of this model to include the effects of the inner snake as well as control and planning strategies that utilize this model to optimize the payload through adjusting the probe shape and/or actuation tendon forces.

REFERENCES

- [1] B. Zhao, L. Zeng, Z. Wu, and K. Xu, "A continuum manipulator for continuously variable stiffness and its stiffness control formulation," *Mechanism and Machine Theory*, vol. 149, p. 103746, 2020.
- [2] J. M. You, H. Kim, J. Kim, and D.-S. Kwon, "Design and analysis of high-stiffness hyperredundant manipulator with sigma-shaped wire path and rolling joints," *IEEE Robotics and Automation Letters*, vol. 6, no. 4, pp. 7357–7364, 2021.
- [3] T. Ota, A. Degani, D. Schwartzman, B. Zubiate, J. McGarvey, H. Choset, and M. A. Zenati, "A novel highly articulated robotic surgical system for epicardial ablation," in *2008 30th Annual International Conference of the IEEE Engineering in Medicine and Biology Society*. IEEE, 2008, pp. 250–253.
- [4] A. Degani, H. Choset, A. Wolf, and M. A. Zenati, "Highly articulated robotic probe for minimally invasive surgery," in *Proceedings 2006 IEEE International Conference on Robotics and Automation, 2006. ICRA 2006*. IEEE, 2006, pp. 4167–4172.
- [5] J. Burgner-Kahrs, D. C. Rucker, and H. Choset, "Continuum robots for medical applications: A survey," *IEEE Transactions on Robotics*, vol. 31, no. 6, pp. 1261–1280, 2015.
- [6] A. Orehkov, C. Abah, and N. Simaan, "Snake-like robots for minimally invasive, single-port, and intraluminal surgeries," *The Encyclopedia of Medical Robotics*. World Scientific, pp. 203–243, 2018.
- [7] P. Dupont, N. Simaan, H. Choset, and C. Rucker, "Continuum robots for medical interventions," *Proceedings of the IEEE*, 2022.
- [8] Da Vinci Surgical System, Instrument and Accessory Catalog. Accessed Sept. 9, 2022. [Online]. Available: http://www.unthsc.edu/patientcare/wp-content/uploads/sites/27/Intuitive_Surgical.ins.cat_1.pdf
- [9] Y.-J. Kim, S. Cheng, S. Kim, and K. Iagnemma, "A novel layer jamming mechanism with tunable stiffness capability for minimally invasive surgery," *IEEE Transactions on Robotics*, vol. 29, no. 4, pp. 1031–1042, 2013.
- [10] P. Berthet-Rayne, G. Gras, K. Leibrandt, P. Wisanuvej, A. Schmitz, C. A. Seneci, and G.-Z. Yang, "The i2Snake robotic platform for endoscopic surgery," *Annals of biomedical engineering*, vol. 46, no. 10, pp. 1663–1675, 2018.
- [11] Y.-J. Kim, S. Cheng, S. Kim, and K. Iagnemma, "A stiffness-adjustable hyperredundant manipulator using a variable neutral-line mechanism for minimally invasive surgery," *IEEE transactions on robotics*, vol. 30, no. 2, pp. 382–395, 2013.
- [12] M. Hwang and D.-S. Kwon, "Strong continuum manipulator for flexible endoscopic surgery," *IEEE/ASME Transactions on Mechatronics*, vol. 24, no. 5, pp. 2193–2203, 2019.
- [13] J. Kim, S.-i. Kwon, Y. Moon, and K. Kim, "Cable-movable rolling joint to expand workspace under high external load in a hyper-redundant manipulator," *IEEE/ASME Transactions on Mechatronics*, vol. 27, no. 1, pp. 501–512, 2021.

- [14] P. Rao, Q. Peyron, S. Lilge, and J. Burgner-Kahrs, "How to model tendon-driven continuum robots and benchmark modelling performance," *Frontiers in Robotics and AI*, vol. 7, p. 630245, 2021.
- [15] M. M. Dalvand, S. Nahavandi, and R. D. Howe, "An analytical loading model for n -tendon continuum robots," *IEEE Transactions on Robotics*, vol. 34, no. 5, pp. 1215–1225, 2018.
- [16] K. Oliver-Butler, J. Till, and C. Rucker, "Continuum robot stiffness under external loads and prescribed tendon displacements," *IEEE Transactions on Robotics*, vol. 35, no. 2, pp. 403–419, 2019.
- [17] P. M. Loschak, S. F. Burke, E. Zumbro, A. R. Forelli, and R. D. Howe, "A robotic system for actively stiffening flexible manipulators," in *2015 IEEE/RSJ International Conference on Intelligent Robots and Systems (IROS)*. IEEE, 2015, pp. 216–221.
- [18] S. Tully, G. Kantor, M. A. Zenati, and H. Choset, "Shape estimation for image-guided surgery with a highly articulated snake robot," in *2011 IEEE/RSJ International Conference on Intelligent Robots and Systems*. IEEE, 2011, pp. 1353–1358.
- [19] A. Faraz and S. Payandeh, "Towards approximate models of coulomb frictional moments in:(i) revolute pin joints and (ii) spherical-socket ball joints," *Journal of engineering mathematics*, vol. 40, no. 3, pp. 283–296, 2001.
- [20] L. Gutkowski and G. Kinzel, "A Coulomb friction model for spherical joints," in *International Design Engineering Technical Conferences and Computers and Information in Engineering Conference*, vol. 9396. American Society of Mechanical Engineers, 1992, pp. 243–250.
- [21] R. Sage, *The mathematical modelling of ball-joints with friction*. University of Leicester (United Kingdom), 1987.